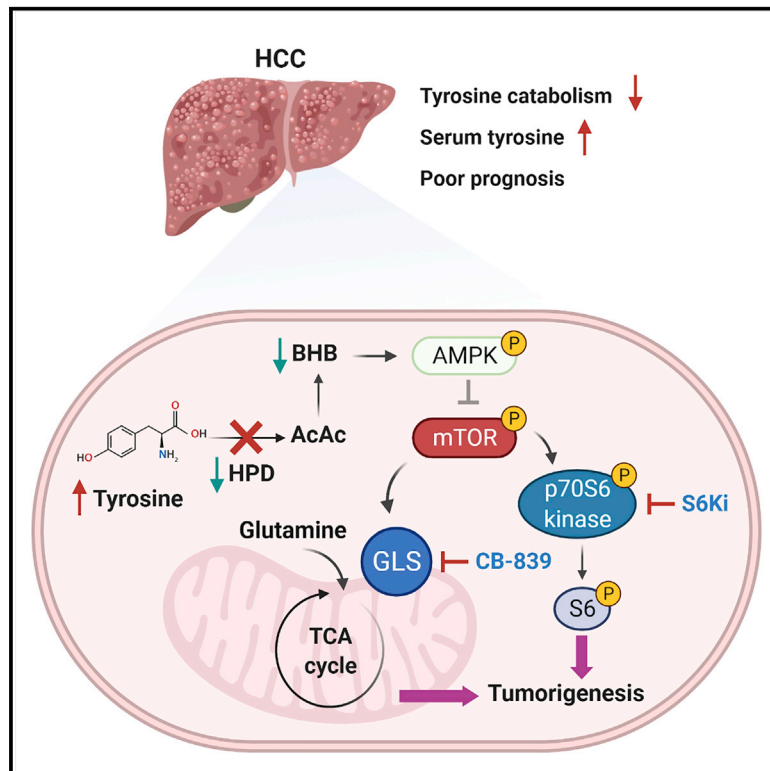# Loss of tyrosine catabolic enzyme HPD promotes glutamine anaplerosis through mTOR signaling in liver cancer

Graphical abstract

Authors

Man Tong, Tin-Lok Wong,
Hongzhi Zhao, ..., Terence Kin-Wah Lee,
Zongwei Cai, Stephanie Ma

Correspondence

caroltm@hku.hk (M.T.),
zwcai@hkbu.edu.hk (Z.C.),
stefma@hku.hk (S.M.)

In brief

Tong et al. report that deranged tyrosine catabolism can predict poor prognosis in human liver cancer. Loss of tyrosine catabolic enzyme HPD promotes glutamine dependency and supports hepatic tumorigenesis, which could be exploited as a metabolic vulnerability for liver cancer treatment.

Highlights

- Loss of HPD promotes cell proliferation and hepatic tumorigenesis

- HPD silencing promotes glutamine anaplerosis through mTOR activation

- Co-targeting p70S6 kinase and glutaminase suppresses hepatic tumors with loss of HPD

- Loss of HPD is predictive of the response to combined metabolic therapy

Article

Loss of tyrosine catabolic enzyme HPD promotes glutamine anaplerosis through mTOR signaling in liver cancer

Man Tong,[1,2,*] Tin-Lok Wong,[1] Hongzhi Zhao,[4] Yuanyuan Zheng,[4] Yu-Nong Xie,[1] Cheuk-Hin Li,[1] Lei Zhou,[1] Noélia Che,[1] Jing-Ping Yun,[5] Kwan Man,[3,6] Terence Kin-Wah Lee,[7] Zongwei Cai,[4,*] and Stephanie Ma[1,2,3,8,*]

[1]School of Biomedical Sciences, Li Ka Shing Faculty of Medicine, The University of Hong Kong, Hong Kong, China
[2]State Key Laboratory of Liver Research, The University of Hong Kong, Hong Kong, China
[3]The University of Hong Kong-Shenzhen Hospital, Shenzhen, China
[4]State Key Laboratory of Environmental and Biological Analysis, Hong Kong Baptist University, Hong Kong, China
[5]Department of Pathology, Sun Yat-Sen University Cancer Center, Guangzhou, China
[6]Department of Surgery, Li Ka Shing Faculty of Medicine, The University of Hong Kong, Hong Kong, China
[7]Department of Applied Biology and Chemical Technology, The Hong Kong Polytechnic University, Hong Kong, China
[8]Lead contact
*Correspondence: caroltm@hku.hk (M.T.), zwcai@hkbu.edu.hk (Z.C.), stefma@hku.hk (S.M.)
https://doi.org/10.1016/j.celrep.2021.109617

SUMMARY

The liver plays central roles in coordinating different metabolic processes, such as the catabolism of amino acids. In this study, we identify a loss of tyrosine catabolism and a concomitant increase in serum tyrosine levels during liver cancer development. Liver cells with disordered tyrosine catabolism, as exemplified by the suppression of a tyrosine catabolic enzyme 4-hydroxyphenylpyruvate dioxygenase (HPD), display augmented tumorigenic and proliferative potentials. Metabolomics profiling and isotope tracing reveal the metabolic reliance of HPD-silenced cells on glutamine, coupled with increased tricarboxylic acid cycle metabolites and their associated amino acid pools. Mechanistically, HPD silencing reduces ketone bodies, which regulate the proliferative and metabolic phenotypes via the AMPK/mTOR/p70S6 kinase pathway and mTOR-dependent glutaminase (GLS) activation. Collectively, our results demonstrate a metabolic link between tyrosine and glutamine metabolism, which could be exploited as a potentially promising anticancer therapy for liver cancer.

INTRODUCTION

Hepatocellular carcinoma (HCC) is the most common form of all primary liver malignancies and represents the third leading cause of cancer-related death globally (Llovet et al., 2016; Bray et al., 2018). Current treatment options for advanced HCC are limited to two main classes of US Food and Drug Administration (FDA)-approved drugs, namely, tyrosine kinase inhibitors and immune checkpoint inhibitors, which only show efficacy in a minority of patients with HCC (Huang et al., 2020). Therefore, the identification of novel causative molecular biomarkers remains a high priority to improve clinical decision-making and the design of novel therapeutic interventions.

Metabolic reprogramming is a major hallmark of cancer (Fouad and Aanei, 2017). Cancer cells undergo huge metabolic alterations to fulfill the energetic, biosynthetic, and redox homeostasis demands of rapidly dividing cells (Pavlova and Thompson, 2016). Despite the importance of metabolic reprogramming in cancer development, only a handful of molecular inhibitors targeting metabolic aberrations in cancer have attained satisfactory outcomes in clinical trials and have been approved by the FDA for clinical use (Mullard, 2017; Liu et al., 2020). The liver is one of the most metabolically active organs in our body and has critical roles

in regulating different metabolic processes (Campbell, 2006). Emerging evidence suggests that metabolic reprogramming of glucose, glutamine, and fatty acids contributes to HCC development and progression (Zhu et al., 2020). Recent genetic profiling indicates that almost 50% of HCC cases display a preponderance of mutations affecting phosphatidylinositol 3-kinase (PI3K)/protein kinase B (AKT)/the mechanistic target of rapamycin (mTOR) signaling (Schulze et al., 2015; Cancer Genome Atlas Research Network, 2017). mTOR serves as a central node to coordinate different metabolic processes and represents a druggable target, as evidenced by multiple early-phase clinical trials in HCC (NCT03059147, NCT01239355, NCT00390195) (Matter et al., 2014). However, single therapy against mTOR often fails to improve clinical outcome, which is attributable to the activation of compensatory pathways (Momcilovic et al., 2018). A limited understanding of the crosstalk of various metabolic pathways and their metabolic link with oncogenic pathways precludes effective therapeutic strategies to target cancer metabolism. In particular, the causative roles of amino acids in functionally driving cancer transformation and cancer development in the liver are not thoroughly characterized.

Tyrosine catabolism occurs primarily in the liver and, to a lesser extent, in the kidney, where tyrosine is metabolized to
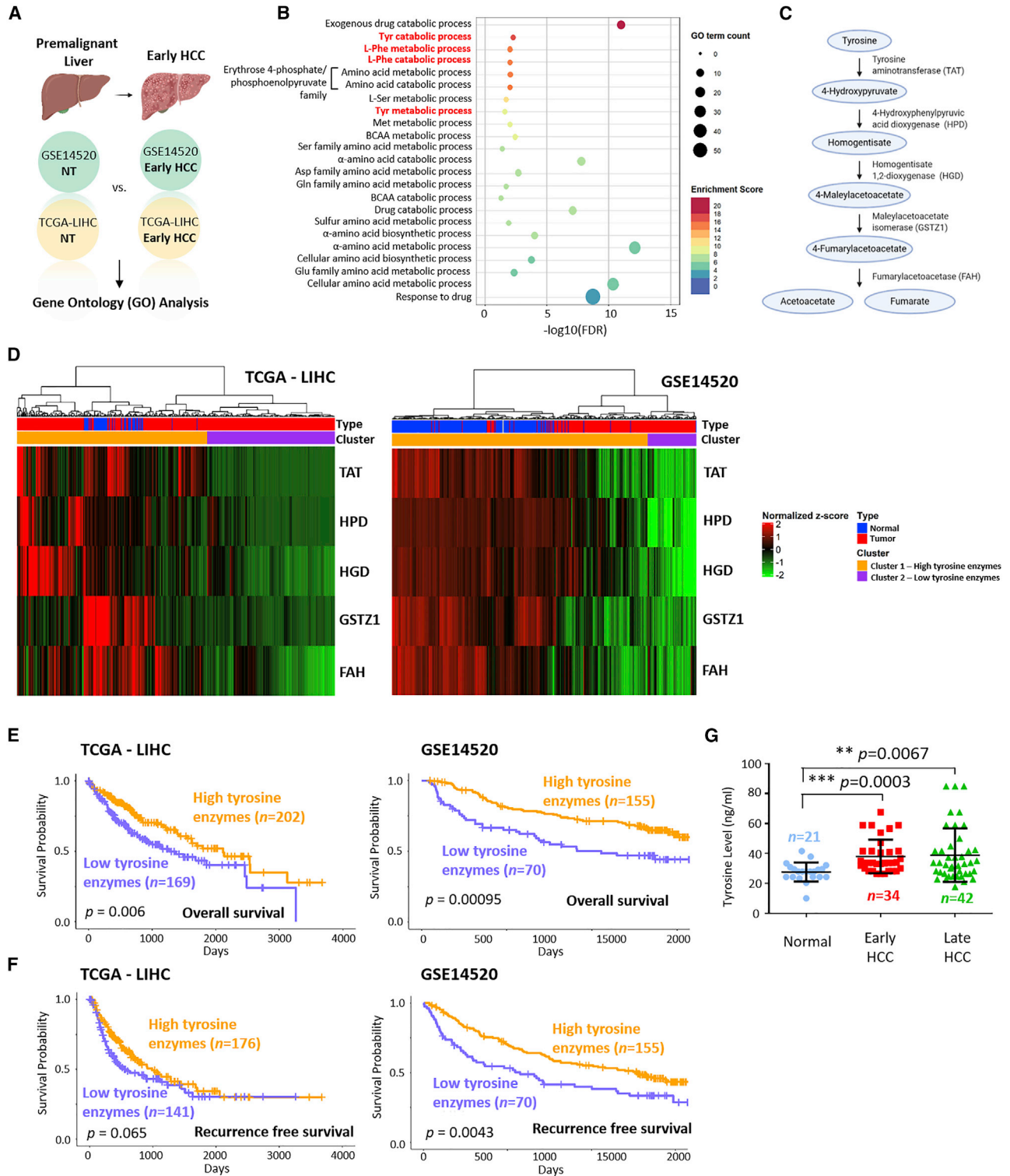
Figure 1. Tyrosine catabolism is suppressed in early-stage HCC, and its deregulation is correlated with dismal patient survival

(A) Schematic of the identification of deregulated pathways in early-stage hepatocellular carcinoma (HCC) versus non-tumor (NT) samples from two publicly available datasets (GSE14520 and The Cancer Genome Atlas-Liver Hepatocellular Carcinoma [TCGA-LIHC]) by Gene Ontology (GO) analysis.

(B) GO enrichment analysis of common deregulated pathways in early-stage HCC samples versus NT samples from two publicly available datasets (GSE14520 and TCGA-LIHC). The colors of the bubble plot indicate normalized enrichment score, and the size of the bubble plot indicates GO term count.

(legend continued on next page)

produce intermediates or precursors for the tricarboxylic acid (TCA) cycle and ketogenesis (Noda and Ichihara, 1976). Tyrosine is catabolized to fumarate and acetoacetate (AcAc) through multiple steps of enzymatic reactions, which are catalyzed by tyrosine aminotransferase (TAT), 4-hydroxyphenylpyruvate dioxygenase (HPD), homogentisate 1,2-dioxygenase (HGD), maleylacetoacetate isomerase (GSTZ1), and fumarylacetoacetase (FAH) (Shiman and Gray, 1998). Mutations in these enzymes, including TAT, HPD, and FAH, have been linked to a metabolic disorder known as tyrosinemia, a condition characterized by elevated blood levels of tyrosine (Scott, 2006; Russo et al., 2001). In patients with chronic liver diseases, an upregulation of serum tyrosine levels has been previously reported (Tajiri and Shimizu, 2013). Deregulation of tyrosine catabolic enzymes has been independently reported in various types of cancers, including HCC (Shan et al., 2019; Wang et al., 2019; Fu et al., 2010; Li et al., 2019; Orejuela et al., 2008; Yang et al., 2019, 2020). Our group has recently reported that loss of the second tyrosine catabolic enzyme HPD is closely associated with poor clinical outcome in HCC (Yang et al., 2020). However, the metabolic consequences of disordered tyrosine catabolism in association with the rewiring of nutrient reliance and adaptation to drive hepatic tumorigenesis remain poorly characterized.

In the present study, we identified a metabolic signature of impaired tyrosine catabolism that is closely associated with poor clinical outcome in HCC. Functionally, silencing of the second tyrosine catabolic enzyme, HPD, promoted tumor formation and cell proliferation. Moreover, HPD-silenced cells displayed increased reliance on glutamine to support enhanced proliferation and mitochondrial respiration. Mechanistically, HPD silencing regulated metabolic alterations through the activation of the ketone-body-dependent AMPK/mTOR pathway. A preclinical immunocompetent mouse HCC model with low HPD expression demonstrated that combinatorial blockade of two downstream mTOR targets, ribosomal protein S6 kinase beta-1 (also known as p70S6 kinase) and glutaminase (GLS), could prolong the survival of mice and reduce tumor burden. The therapeutic efficacy of this combinatorial treatment was further confirmed using human patient-derived organoids with a complete loss of HPD expression.

RESULTS

Impaired tyrosine catabolism, as a common metabolic pathway deregulated in human HCC, portends poor prognosis

In search of common deregulated pathways involved in HCC development, we utilized two publicly available datasets

(GSE14520 and The Cancer Genome Atlas-Liver Hepatocellular Carcinoma [TCGA-LIHC]) that are comprised of both Asian and white ethnicities for pathway enrichment analysis. To identify the most enriched pathways that contribute to the early development of HCC, lists of differentially expressed genes (DEGs) in TCGA-LIHC and GSE14520 cohorts were curated by comparing early-stage HCC versus non-tumor tissues, with an adjusted p value < 0.01 and a log fold change > 1 or < −1 (Figure 1A). Gene Ontology (GO) enrichment analysis of GO biological processes and subsequent clustering of GO terms resulted in an enriched cluster related to amino acid metabolism (Figure 1B). Among the enriched amino acid metabolic processes, tyrosine metabolism and its closely related phenylalanine metabolism were ranked as the most significant deregulated amino acid metabolism pathways between early-stage HCC and non-tumor liver (Figures 1B and 1C). Importantly, this metabolic signature of deregulated tyrosine catabolism as a whole was significantly correlated with poor overall survival and recurrence-free survival in patients with HCC (Figures 1D–1F). We also extended our analysis to the blood, where we found that low expression of tyrosine catabolic enzymes resulted in high serum tyrosine readouts in both early-stage and late-stage patients with HCC compared with normal and healthy individuals (Figure 1G). Overall, these data suggest that impaired tyrosine catabolism is clinically relevant to the early development of HCC and that this deregulated metabolic signature can be used as a potential diagnostic and prognostic marker for HCC.

HPD silencing promotes cell proliferation and tumorigenesis

To examine the functional and metabolic consequences of impaired tyrosine catabolism, we manipulated the expression and activity of the second tyrosine catabolic enzyme, HPD, of which we recently reported its clinical importance in human HCC (Yang et al., 2020). We examined HPD expression in a panel of normal liver and liver cancer cell lines (Figure 2A). Compared with the immortalized normal liver epithelial cell line MIHA and the hepatoblastoma cell line HepG2, all six liver cancer cell lines (Hep3B, Huh7, PLC/PRF/5, HLE, MHCC97L, and MHCC97H) tested had markedly lower or undetectable levels of HPD expression, with a similar trend observed across both genomic and proteomic levels (Figure 2A). To understand the role of impaired tyrosine catabolism in hepatic tumorigenesis, we manipulated the expression of HPD in HepG2 and PLC/PRF/5 cells, which showed high and no/low HPD expression, respectively (Figure 2A). HPD-depleted HepG2 cells displayed enhanced cell proliferation capacity compared with the

(C) Biochemical pathway of tyrosine catabolism showing the intermediate metabolites and the enzymes involved in each step of tyrosine breakdown.

(D) Hierarchical clustering of five tyrosine catabolic enzyme transcript levels across HCC and NT liver tissues in TCGA-LIHC (left) and GSE14520 (right) datasets. Patients are segregated into two clusters: cluster 1, high tyrosine enzymes and cluster 2, low tyrosine enzymes.

(E) Kaplan-Meier survival estimate curves for overall survival of patients with HCC with high or low tyrosine enzymes as defined by the clusters in TCGA-LIHC (left) and GSE14520 (right) datasets.

(F) Kaplan-Meier survival estimate curves for recurrence free survival of patients with HCC with high or low tyrosine enzymes as defined by the clusters in TCGA-LIHC (left) and GSE14520 (right) datasets.

(G) Tyrosine levels in blood serum samples collected from healthy individuals (normal) (n = 21) and early-stage (n = 34) and late-stage (n = 42) patients with HCC. Data are represented as mean ± SD.
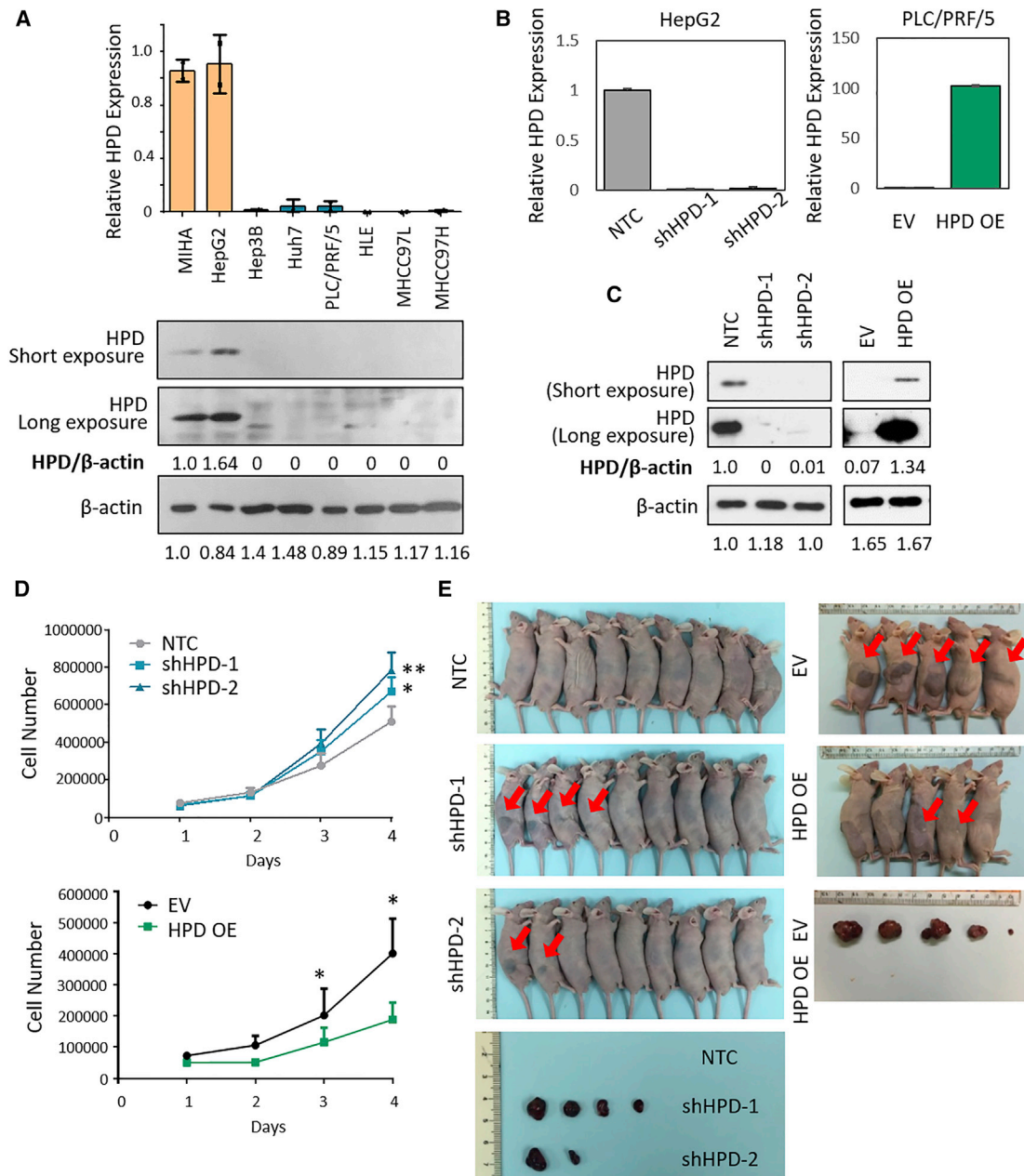
*p < 0.01; **p < 0.001.

ns, not significant.

Figure 2. Deletion of tyrosine catabolic enzyme HPD promotes cell proliferation and tumorigenesis

(A) Genomic (top) and proteomic (bottom) HPD expression in a panel of immortalized normal liver MIHA, hepatoblastoma HepG2, and HCC cell lines (Hep3B, Huh7, PLC/PRF/5, HLE, MHCC97L, and MHCC97H) by real-time qPCR and western blot analyses.

(B) Validation of HPD expression in HepG2 cells with lentiviral-transduced non-target control (NTC) and HPD short hairpin RNAs (shRNAs) (shHPD-1 and shHPD-2), and PLC/PRF/5 cells with lentiviral-transduced empty vector (EV) and HPD overexpression (HPD OE) plasmids by qPCR analyses.

(C) Western blot analyses of HPD expression in HepG2 cells HPD silencing and PLC/PRF/5 cells with HPD OE.

(D) Cell proliferation curves of HepG2 NTC cells and HPD shRNA clones (top) and PLC/PRF/5 EV and HPD OE cells (bottom).

(E) Representative images of the xenograft tumors formed in nude mice following injection of HepG2 NTC cells and HPD shRNA clones (left) (n = 9 mice per group) and PLC/PRF/5 EV and HPD OE cells (right) (n = 5 mice per group).

Graphs include all data points and mean ± SD (n = 3 independent experiments with 3 technical replicates in each experiment). *p < 0.05; **p < 0.01.

respective control cells (Figures 2B and 2C). Additionally, HPD silencing initiated tumor development in immunosuppressive mice (Figure 2D). By contrast, overexpression of HPD in PLC/PRF/5 cells attenuated cell proliferation and tumorigenesis (Figures 2B–2D). As a complementary approach, we utilized nitisinone (NTBC), a recognized compound that specifically blocks
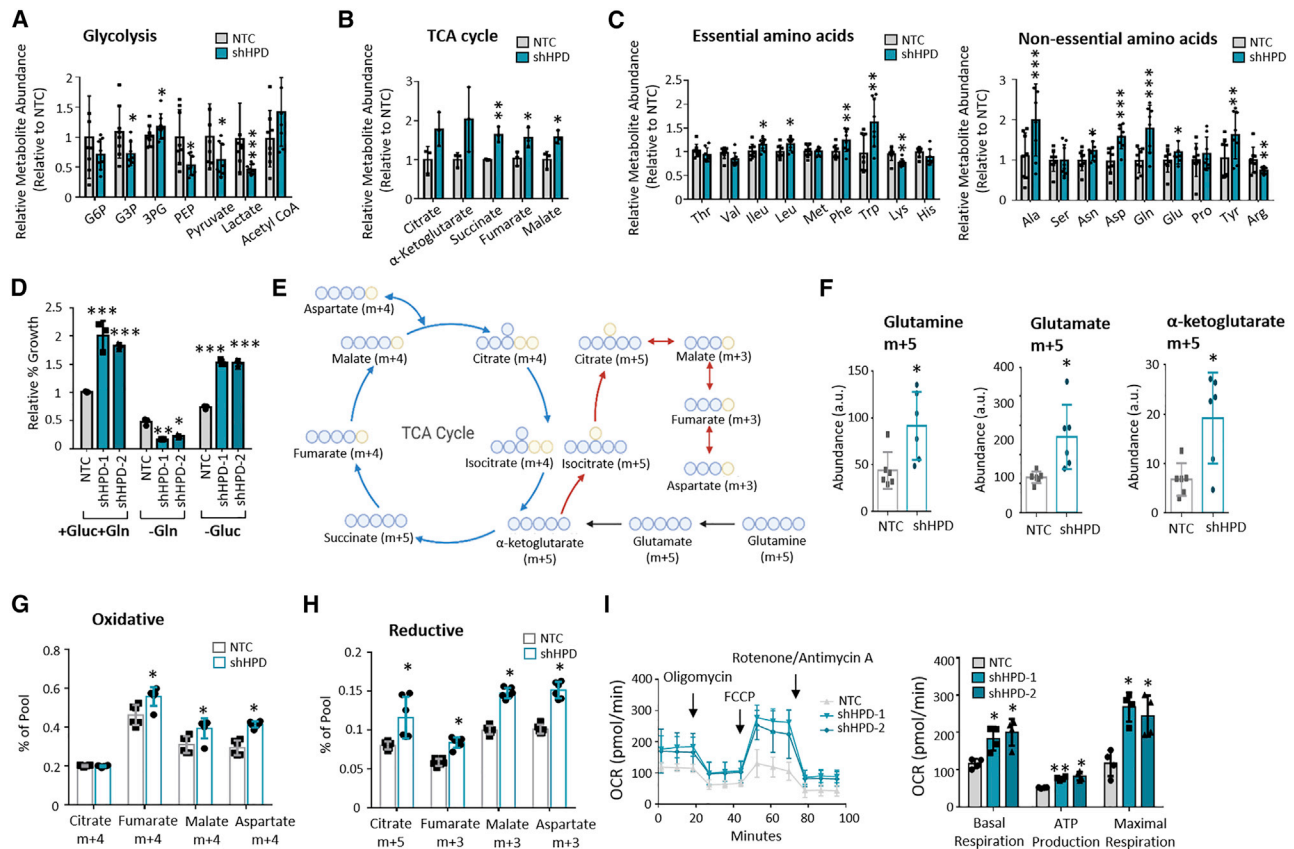
Figure 3. HPD deletion increases TCA cycle and amino acid pools and promotes glutamine flux into TCA cycle

(A–C) Quantification of glycolytic metabolites (A), TCA cycle metabolites (B), and amino acids (C) in HepG2 NTC cells and HPD shRNA clones by LC-MS.

(D) Percentage of growth of HepG2 NTC cells and HPD shRNA clones under glutamine (−Gln) or glucose (−Gluc) deprivation.

(E) Schematic of isotopomer conversion from $^{13}C_5$-Gln.

(F) Graphs representing the metabolite abundance of Gln (M5) (left), glutamate (M5) (middle), and α-ketoglutarate (M5) (right) in HepG2 NTC cells and HPD shRNA clone.

(G) Graph representing percent oxidative derivatives of glutamine including M4-labeled citrate, fumarate, malate, and aspartate in HepG2 NTC cells and a HPD shRNA clone.

(H) Graph representing percent reductive derivatives of glutamine including M5-labeled citrate and M3-labeled fumarate, malate, and aspartate in HepG2 NTC cells and a HPD shRNA clone.

(I) Seahorse MitoStress analyses of HepG2 NTC cells and HPD shRNA clones. Charts show the basal respiration, ATP production, and maximal respiration levels. Graphs include all data points and mean ± SD (n = 6 biological replicates in A to H; n = 3 independent experiments with 3 technical replicates in each experiment in I). * $p < 0.05$; ** $p < 0.01$; *** $p < 0.001$.

a.u., arbitrary unit; OCR, oxygen consumption rate.

HPD enzymatic activities. Treating HepG2 cells with NTBC similarly caused an increase in cell proliferation (Figure S1A). Overall, HPD plays a critical tumor suppressive role in HCC.

LC-MS metabolic profiling of HPD-deficient HCC cells identifies a high abundance of TCA cycle and amino acid metabolites

It was then explored whether enhanced proliferation capacity parallels the abundance of amino acids and the metabolites involved in glycolysis and the TCA cycle in HPD-depleted cells. We performed targeted metabolomics with liquid chromatography-mass spectrometry (LC-MS) to measure metabolite abundance after HPD silencing and HPD overexpression. Glycolytic intermediates, including glucose-6-phosphate (G6P), glyceral-

dehyde-3-phosphate (G3P), phosphoenolpyruvate (PEP), pyruvate, and lactate, showed significant decreases or trending decreases in levels when HPD was depleted (Figure 3A). Intriguingly, TCA cycle intermediates, including citrate, α-ketoglutarate, succinate, fumarate, and malate, were significantly increased or trending toward increase in HPD-depleted cells (Figure 3B). While fumarate is one of the end products of tyrosine catabolism, it was unexpected that fumarate levels increased in HPD-depleted cells. The intracellular amino acid levels were also quantified (Figure 3C). The levels of tyrosine were upregulated in HPD-depleted cells, demonstrating that depletion of HPD leads to impaired tyrosine catabolism and accumulation of tyrosine. Phenylalanine, which can be converted to tyrosine by phenylalanine hydrolase, also had an increased level in HPD-depleted

cells, suggesting impaired tyrosine catabolism leading to reduced hydroxylation of phenylalanine to tyrosine. The nonessential amino acids (Ala, Asn, Asp, Gln, and Glu), which are associated with the TCA cycle, showed concomitant increased levels in HPD-depleted cells. Branched chain amino acids (BCAAs: Val, Ileu, and Leu) showed varying levels in HPD-depleted cells. By contrast, HPD-overexpressing cells had reduced levels of TCA cycle metabolites and amino acids (Figures S2A–S2D).

HPD-depleted cells display increased glutamine reliance and glutamine flux to support cell proliferation and mitochondrial respiration

We next investigated whether and how nutrient availability affects the proliferative capacity of HPD-suppressed cells. Glucose and glutamine are the major metabolites used by mammalian cells for ATP production to support cellular activities (Palm and Thompson, 2017). Withdrawal of glucose from the culture medium suppressed cellular growth to a similar extent in both HPD-suppressed cells and the respective control cells (Figures 3D and S1B). By contrast, glutamine withdrawal caused a greater extent of inhibition of proliferation in HPD-suppressed cells than in control cells (Figures 3D and S1B), suggesting that the enhanced proliferative potential driven by loss of HPD is dependent on the presence of glutamine. Contrary to the increased glutamine dependency observed in HPD-suppressed cells, HPD-overexpressing cells did not preferentially rely on glutamine for proliferation (Figure S2E). Complementary to the deprivation of glutamine in the medium, blockade of glutamine uptake by inhibiting glutamine transporter SLC1A5 with GPNA (L-γ-glutamyl-p-nitroanilide) similarly suppressed cell proliferation of HPD-suppressed cells (Figure S3A), indicating a high metabolic dependency on glutamine.

To better explore the glutamine flux and the metabolic fates of glutamine in HPD-depleted cells, we performed an MS-based stable isotope tracing study using uniformly labeled $^{13}C_5$-glutamine (U-$^{13}C_5$-glutamine) (Figure 3E). Significantly higher levels of fully labeled (M5) glutamine, glutamate, and α-ketoglutarate derived from $^{13}C_5$-glutamine were detected in HPD-depleted cells (Figure 3F). Both oxidative and reductive derivatives of glutamine, including citrate, fumarate, malate, and aspartate, showed increased levels in HPD-depleted cells (Figures 3G and 3H), suggesting that enhanced reliance on glutamine serves as an anaplerotic source to replenish TCA cycle intermediates, which may also explain the increased fumarate abundance in HPD-depleted cells. Concomitant with an increase in glutamine flux through the TCA cycle, mitochondrial respiratory capacity and ATP production were increased in HPD-suppressed cells, and reversed phenotypes were observed in HPD-overexpressing cells (Figures 3I and S2F). Inhibition of glutamine uptake by GPNA consistently demonstrated that increased mitochondrial respiration driven by HPD suppression depended on glutamine availability (Figure S3B).

Ketone bodies as a direct downstream metabolic regulator in HPD-suppressed HCC

Apart from converting into fumarate, tyrosine is also a source of ketone bodies and breaks down into AcAc in the liver (Shiman and Gray, 1998). AcAc rapidly converts to acetone, which is

excreted in the breath or urine, and it also converts to a more stable form, β-hydroxybutyrate (BHB), by the enzyme BHB dehydrogenase in the liver (Shiman and Gray, 1998). We next investigated the contributions of these ketone bodies in regulating the metabolic functions of HPD in the liver. Because of its instability, we detected a minimal level of AcAc, and no significant difference was observed between HPD-depleted cells, HPD-overexpressing cells, and their respective control cells (Figures 4A and S2G). HPD silencing, however, resulted in a reduced abundance of BHB (Figure 4B). Increased BHB levels were detected in HPD-overexpressing cells (Figure S2H). Rescue treatment with BHB reversed the metabolic phenotypes resulting from HPD suppression, leading to reduced cell proliferation and mitochondrial respiration (Figures 4C and 4D). Intriguingly, rescue treatment with AcAc likewise resulted in phenotypes similar to those observed with BHB treatment (Figures 4C and 4D), likely through conversion to BHB. The regulatory roles of AcAc and BHB in cell proliferation and mitochondrial respiration indicate that ketone bodies are the direct downstream metabolic regulator of tyrosine catabolism.

HPD suppression activates mTOR and its downstream p70S6K/S6 and c-MYC/GLS signaling axes

We next sought to investigate the altered signaling pathways driven by the loss of tyrosine catabolism in HCC. Gene set enrichment analysis (GSEA) pathway enrichment showed that PI3K/AKT/mTOR and mTOR Complex 1 (mTORC1) signaling were significantly enriched in patients with HCC with low expression of tyrosine enzymes in the TCGA-LIHC dataset (Figure 5A). AMP-activated protein kinase (AMPK) is widely recognized as an mTORC1 antagonist that is activated during low-energy conditions (Hindupur et al., 2015). Consistent with an increased respiratory capacity and ATP production, as demonstrated by Seahorse analysis, HPD-suppressed cells showed reduced phosphorylated AMPK (p-AMPK) (Figures 5B and S1D), indicating a high energy status. The expression of phosphorylated mTOR (p-mTOR) and its downstream targets, including phosphorylated p70S6 kinase (p-p70S6K) and phosphorylated S6 (p-S6), was increased in HPD-suppressed cells compared with control cells (Figures 5B and S1D). By contrast, active AMPK and suppressed mTOR signaling were observed in HPD-overexpressing PLC/PRF/5 cells (Figure 5B). To identify the molecular target that contributes to the enhanced glutamine reliance and glutamine flux driven by HPD suppression, we performed correlation analysis of HPD expression with the expression of genes related to glutamine metabolism and the TCA cycle. Kidney-type GLS (GLS) was identified as the gene most negatively correlated with HPD, while liver-type GLS (GLS2) and glutamine synthetase (GLUL or GS) showed a positive correlation with HPD in the TCGA-LIHC dataset (Figure 5C). GLS is the enzyme hydrolyzing glutamine to form glutamate as part of the glutaminolysis pathway, whereas GS is the enzyme catalyzing the reversal step of glutamine hydrolysis, thus converting glutamate back to glutamine (Bott et al., 2019). We examined the proteomic expression of the two GLS isoenzymes and GS in HPD-depleted cells and found that GLS expression was increased, while GLS2 and GS expression was decreased when HPD was depleted (Figure S4). GLS is a downstream target of mTOR, and its
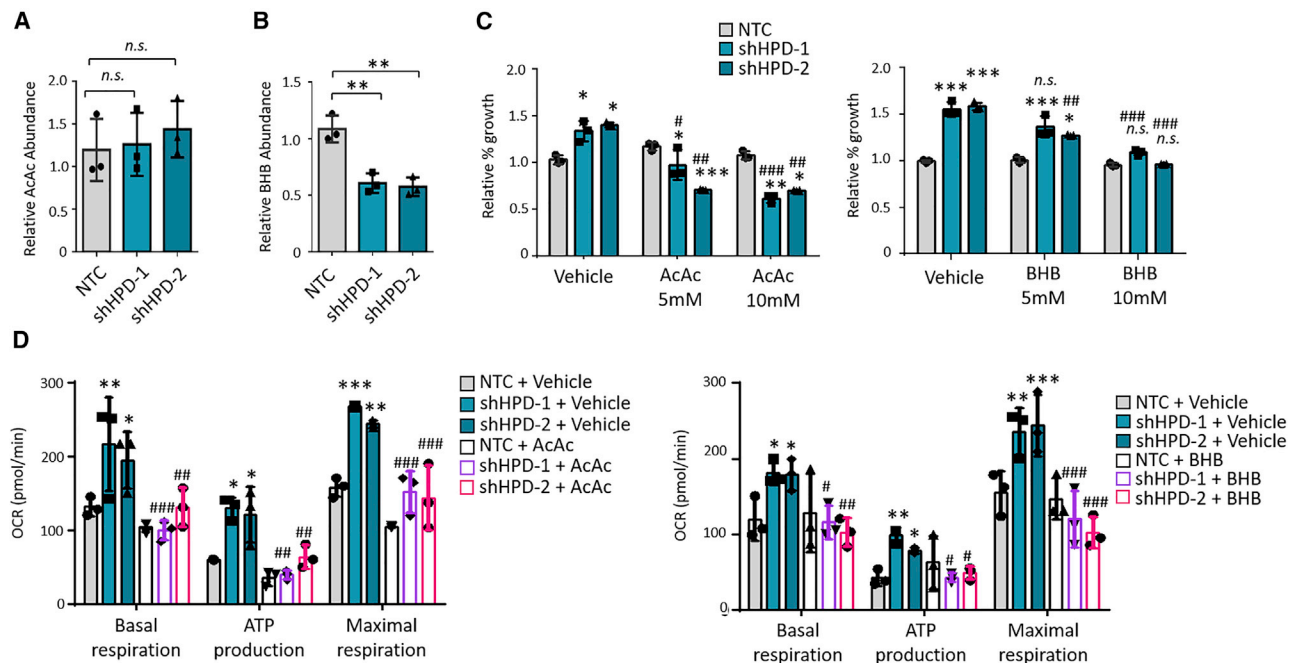
Figure 4. Ketone bodies derived from tyrosine catabolism regulate the metabolic phenotypes driven by HPD deletion

(A and B) Relative abundance of (A) acetoacetate (AcAc) and (B) β-hydroxybutyrate (BHB) in NTC cells and HPD shRNA clones derived from HepG2 cells.

(C) Percentage of growth of HepG2 NTC cells and HPD shRNA clones after AcAc (left) and BHB (right) treatment.

(D) Seahorse MitoStress analyses of NTC cells and HPD shRNA clones after AcAc (10 mM, top) and BHB (10 mM, bottom) treatment. Charts show the basal respiration, ATP production, and maximal respiration levels.

Graphs include all data points and mean ± SD (n = 3 independent experiments with 3 technical replicates in each experiment). *p < 0.05; **p < 0.01; ***p < 0.001 (under same treatment group). #p < 0.05; ##p < 0.01; ###p < 0.001 (under same sample versus vehicle treatment).
ns, not significant.

expression is regulated by mTOR-dependent activation of c-MYC (Csibi et al., 2014). We confirmed that the increased expression of c-MYC and GLS was dependent on mTOR activation and that their expression was reduced upon rapamycin treatment in HPD-depleted cells (Figure 5D). We further showed that activation of AMPK/mTOR signaling and its two downstream branches involving the p-S6 and c-MYC/GLS signaling axes was suppressed in HPD-depleted cells with rescue treatment with AcAc and BHB (Figure 5E). A previous study reported the modulation of AMPK activation by BHB (Bae et al., 2016). Our data confirmed that reduced ketone bodies driven by HPD suppression suppress AMPK activation and in turn activate mTOR and its downstream effectors. Interestingly, GLS2 and GS expression was not altered under rapamycin treatment, but their expression was increased upon rescue treatment with AcAc and BHB, suggesting their expression to be regulated by other mechanisms driven by ketone bodies (Figures 5D and 5E).

Combinatorial inhibition of p70S6K and GLS exerts synergistic growth inhibition effects in human HCC patient-derived organoids

The current data raised interest in exploring the therapeutic potential of treating tyrosine-catabolism-impaired HCC with inhibitors targeting the mTORC1 pathway. Over the past decades, multiple mTORC1 inhibitors, including rapamycin and rapalogs such as everolimus, have shown limited therapeutic limitations

in cancers, including HCC (Matter et al., 2014; Formisano et al., 2020). This can be attributable to the reactivation of mTORC1-regulated negative feedback loops. Multiple studies have reported that mTORC1 inhibition with rapamycin releases the feedback inhibition of insulin receptor substrate 1 (IRS-1)/PI3K/AKT signaling, thus causing the adaptive activation of AKT and its downstream signaling to resist rapamycin-mediated growth inhibition (Formisano et al., 2020; O'Reilly et al., 2006; Momcilovic et al., 2018). In cancer patients treated with everolimus, adaptive activation of the mitogen-activated protein kinase (MAPK) signaling cascade was observed under a PI3K-mediated feedback loop (Carracedo et al., 2008). In a study that compared direct mTORC1 inhibition by rapamycin and p70S6K inhibition, surprisingly, AKT phosphorylation was not increased or altered after pharmacological inhibition of p70S6K; AKT phosphorylation was even decreased when p70S6K was knocked down (Wang et al., 2017). Although the underlying mechanism of how p70S6K inhibition does not induce the feedback activation of AKT signaling as observed in mTORC1 inhibition was not examined, the result from this study gave insight into our study, where we therefore chose to use a p70S6K inhibitor (S6Ki, LY2584702) in the hope of minimizing the potential resistance developed and the AKT reactivation from using mTORC1 inhibitors.

Given the increased nutrient dependency of glutamine caused by the activation of GLS, we hypothesized that co-targeting GLS and p70S6K could exert a maximal inhibitory effect in
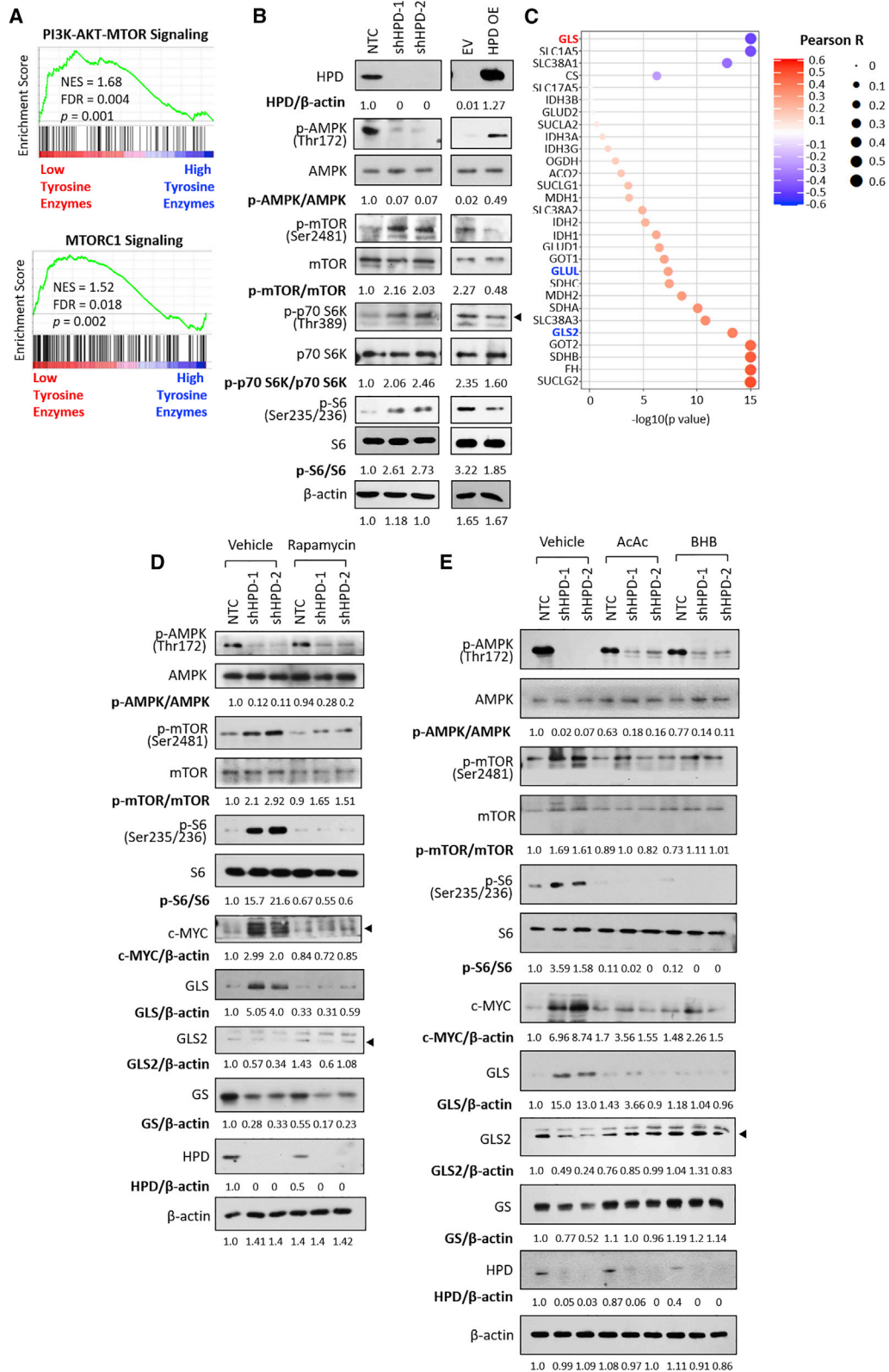
suppressing HCC with loss of HPD or deregulated tyrosine catabolism. To test the therapeutic efficacy of combinatorial treatment with S6Ki and the GLS inhibitor CB-839 in the clinical setting, we utilized HCC patient-derived organoids, which better mimic the pathophysiology of HCC, to test for a therapeutic response. Among the four organoid lines that were established by us and our collaborator, only HCC#3 showed mild expression of HPD, while the other three organoid lines showed undetectable HPD expression (Figure 6A). The baseline levels of GLS, c-MYC, and mTORC1 pathway proteins were also examined (Figure 6A). Dose-response experiments showed that S6Ki at concentrations as high as 5 μM or above caused complete inhibition of p-S6 (Figure S5A) in organoid lines without HPD expression. HCC#3, with modest HPD expression, showed the least sensitivity toward S6Ki treatment, in which p-S6 expression could not be suppressed completely even when 20 μM was added (Figure S5A). We examined the glutamine dependencies of all four lines of organoids and found that HCC#3 with mild HPD expression did not rely on glutamine for growth (Figure 6B). Single treatment with either S6Ki or CB-839 showed a mild suppression of cell proliferation, while the combinatorial treatment resulted in a synergistic inhibition in organoids that did not express HPD (Figures 6C and S5B). However, no synergism was observed in the HCC#3 organoids that showed mild HPD expression (Figure 6C). HCC#2 and HCC#4 organoid lines, which had undetectable HPD expression and strong mTOR activation, showed synergistic inhibitory responses on mitochondrial respiratory capacity toward the combinatorial treatment (Figures 6A, 6D, S5C, and S5D). HCC#1 with weaker mTOR activation only showed additive inhibitory effect when compared with HCC#2 and HCC#4 under combinatorial treatment (Figures 6A, S5C, and S5D). We speculate that the discrepancy in the drug responses may be attributable to stronger mTOR activation with lower p-AMPK and higher p-mTOR, p-p70S6K, and p-S6 observed in HCC#2 and HCC#4 when compared with HCC#1 (Figure 6A). Western blot results showed that the p-S6 and c-MYC/GLS pathways were suppressed after combinatorial treatment in all organoids except HCC#3 (Figures 6E and S5E). Overall, these data suggest that HCC with a complete loss of HPD and strong mTOR activation is more responsive to p70S6K and GLS inhibition.

Blockade of p70S6K and GLS exhibits antitumor effects in a preclinical immunocompetent HCC mouse model with HPD downregulation

HPD expression was reduced in tumors of multiple HCC models, with the most prominent downregulation observed in an HCC model induced by hydrodynamic tail vein injection with plasmids carrying the oncogenes neuroblastoma Ras viral oncogene homolog (NRAS^{V12}) and myristoylated AKT (AKT^{myr}) (Figure 7A). Significant and prominent downregulation of *Hpd* was detected in the liver at 2 weeks postinjection with the plasmids (Figure 7B) when the tumors started to grow and resembled early-stage HCC, according to our previous publication (Tong et al., 2018). We next evaluated the antitumor effect of these inhibitors on liver tumorigenesis (Figure 7C). While single treatment with either S6Ki or CB-839 had no effect on tumor growth, combination treatment with S6Ki and CB-839 significantly reduced the liver-to-body weight ratio and prolonged the survival of the mice (Figures 7D–7F). Immunohistochemistry analysis revealed that the combination treatment reduced cell proliferation with a lower proliferating cell nuclear antigen (PCNA) expression, increased apoptosis with a higher cleaved caspase 3 expression, and reduced p-S6, c-MYC, and GLS expression (Figure 7G). Collectively, our data identified a deregulated metabolic signature driven by loss of tyrosine catabolism that predicts a positive response to combined mTOR/p70S6K and GLS inhibition.

DISCUSSION

The liver is the predominant organ where tyrosine catabolism takes place, which expresses the highest expression of tyrosine catabolic enzymes among other organs (Shiman and Gray, 1998). A recent study similarly reported the downregulation of tyrosine catabolic genes in HCC by comparing various publicly available datasets (Nguyen et al., 2020). However, these authors claimed that the expression of tyrosine catabolic genes was only significantly changed in late-stage HCC, but not in early-stage HCC, based on one independent GEO dataset. In our present study, we stratified the patients into early-stage and late-stage HCC according to the Barcelona Clinic Liver Cancer (BCLC) staging classification (Kinoshita et al., 2015) and compared DEGs between non-tumor and early-stage HCC tissues in both TCGA-LIHC and GSE14520 datasets. Our analysis showed that tyrosine catabolism is an early deregulated metabolic event that is significantly altered between non-tumor and early HCC. More intriguingly, we observed a significant elevation in circulating tyrosine levels in both early- and late-stage patients with HCC, suggesting that impaired tyrosine catabolism is an early event that contributes to HCC transformation and development. In extrahepatic tissues, deregulation of tyrosine catabolic enzymes has also been implicated in various types of cancers. HPD has been reported to be overexpressed and to possess tumorigenic roles in breast and lung cancers (Shan et al., 2019;

Figure 5. HPD regulates ketone-bodies-dependent mTOR activation and promotes mTOR-driven p70S6 kinase and GLS signaling axes

(A) GSEA pathway enrichment analyses of five tyrosine catabolism enzyme signature in patients with HCC from the TCGA-LIHC dataset.

(B) Immunoblots of AMPK/mTOR pathway in HepG2 EV and shHPD clones (left) and PLC/PRF/5 EV and HPD OE cells (right).

(C) Plot showing the expression correlation analyses between HPD and the genes related to glutamine metabolism and TCA cycle in NT liver and HCC tissues from publicly available dataset TCGA-LIHC. Red color of the bubble plot indicates positive correlation, and blue color indicates negative correlation. The size of the bubble plot indicates Pearson R value.

(D) Immunoblots of AMPK/mTOR signaling and glutamine-metabolism-related enzymes in HepG2 NTC and HPD shRNA clones after rapamycin (100 nM) treatment.

(E) Immunoblots of AMPK/mTOR signaling and glutamine-metabolism-related enzymes in HepG2 NTC and HPD shRNA clones after AcAc (10 mM) or BHB (10 mM) treatment.
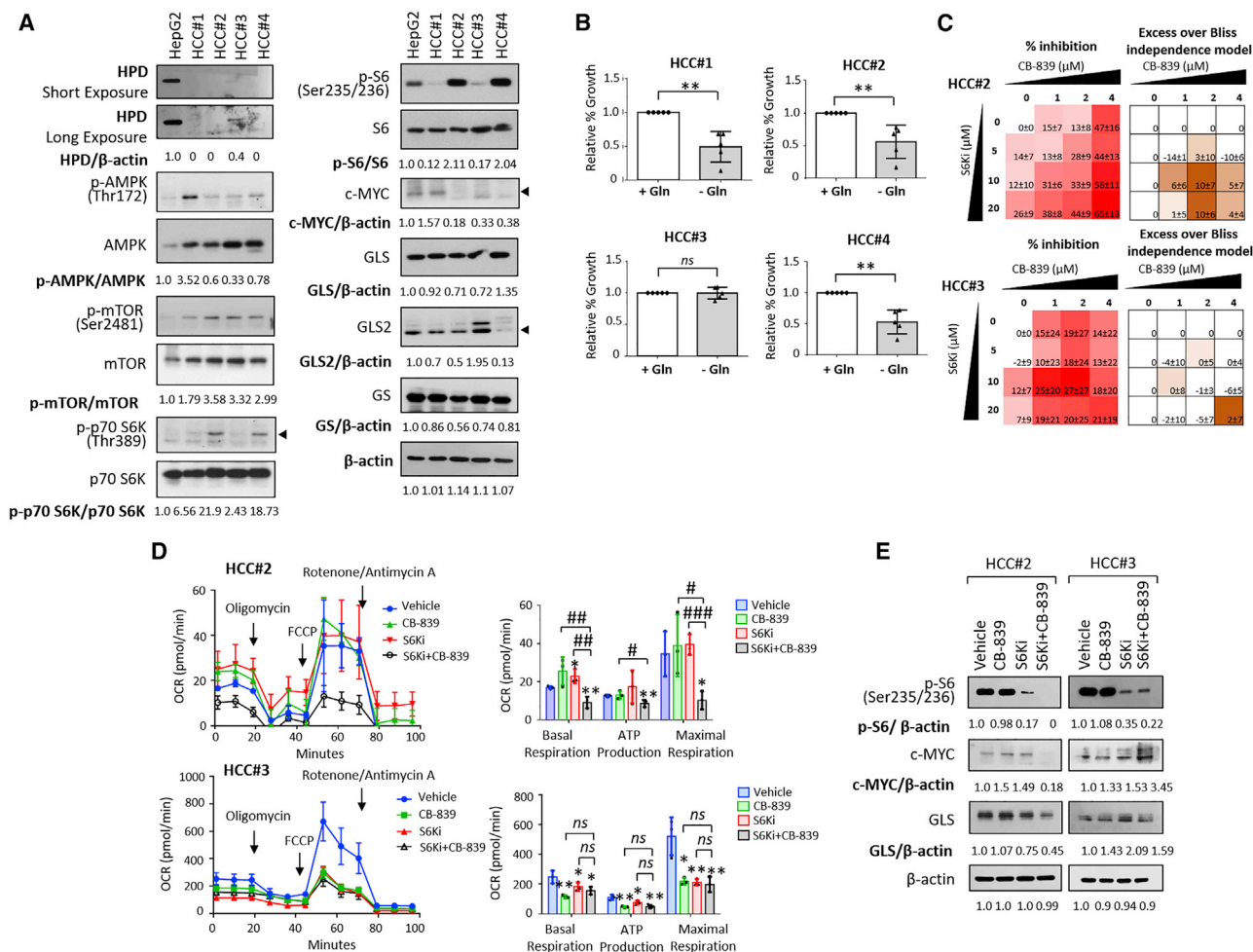
Figure 6. Combination treatment of p70S6 kinase and GLS inhibition exerts synergistic growth inhibition effect in human HCC organoids with HPD downregulation

(A) Immunoblots of HPD, AMPK/mTOR signaling, and glutamine-metabolism-related enzymes in HepG2 cells and four human HCC patient-derived organoids (HCC#1–4).

(B) Graphs representing the percentage of growth of HCC patient-derived organoids in glutamine-depleted medium.

(C) Growth inhibition of HCC#2 and HCC#3 organoids under treatment of increasing doses of S6K inhibitor (S6Ki, LY2584702) and GLS inhibitor (CB-839). The calculated excess inhibition over the predicted Bliss independence is shown for each drug-combination pair.

(D) Seahorse MitoStress analyses of HCC#2 (S6Ki, 20 μM and CB-839, 2 μM) and HCC#3 (S6Ki, 20 μM and CB-839, 4 μM) organoids under S6Ki or CB-839 treatment alone or in combination for 72 h. Charts show the basal respiration, ATP production, and maximal respiration levels.

(E) Immunoblots of p-S6, c-MYC, and GLS in HCC organoids HCC#2 and HCC#3 following single or combination treatment of S6Ki and CB-839.

Graphs include all data points and mean ± SD (n = 3 independent experiments with 3 technical replicates in each experiment in B to D). *p < 0.05; **p < 0.01 (versus vehicle treatment). #p < 0.05 (single versus combination treatment).

Veh, vehicle; ns, not significant.

Wang et al., 2019). HPD is overexpressed in human breast cancer, and its tight correlation with poor overall survival in patients with breast cancer suggested HPD to be a potential prognostic marker (Shan et al., 2019). In lung cancer, HPD is also highly upregulated and correlated with poor prognosis in patients with lung cancer (Wang et al., 2019).

Despite various studies revealing the downregulation of tyrosine catabolic enzymes in HCC, the altered metabolic phenotypes resulting from impaired tyrosine catabolism and the direct metabolic and mechanistic link that promotes HCC tumorigenesis have not been explored to date. In this study, we showed

that HPD deletion increased the TCA cycle and its associated amino acid metabolites, which is supported by increased dependency and flux of glutamine as an anaplerotic source to the TCA cycle. The mechanistic pathway contributing to the altered metabolic phenotypes and glutamine reliance was found to be associated with reduced ketone bodies, thereby activating the mTOR signaling pathway and its downstream effectors p70S6K and GLS. In other cancers where HPD is highly upregulated, the metabolic phenotypes and changes mediated by HPD deregulation are completely different. One study reported that HPD functions as an oncogene to promote lung cancer cell
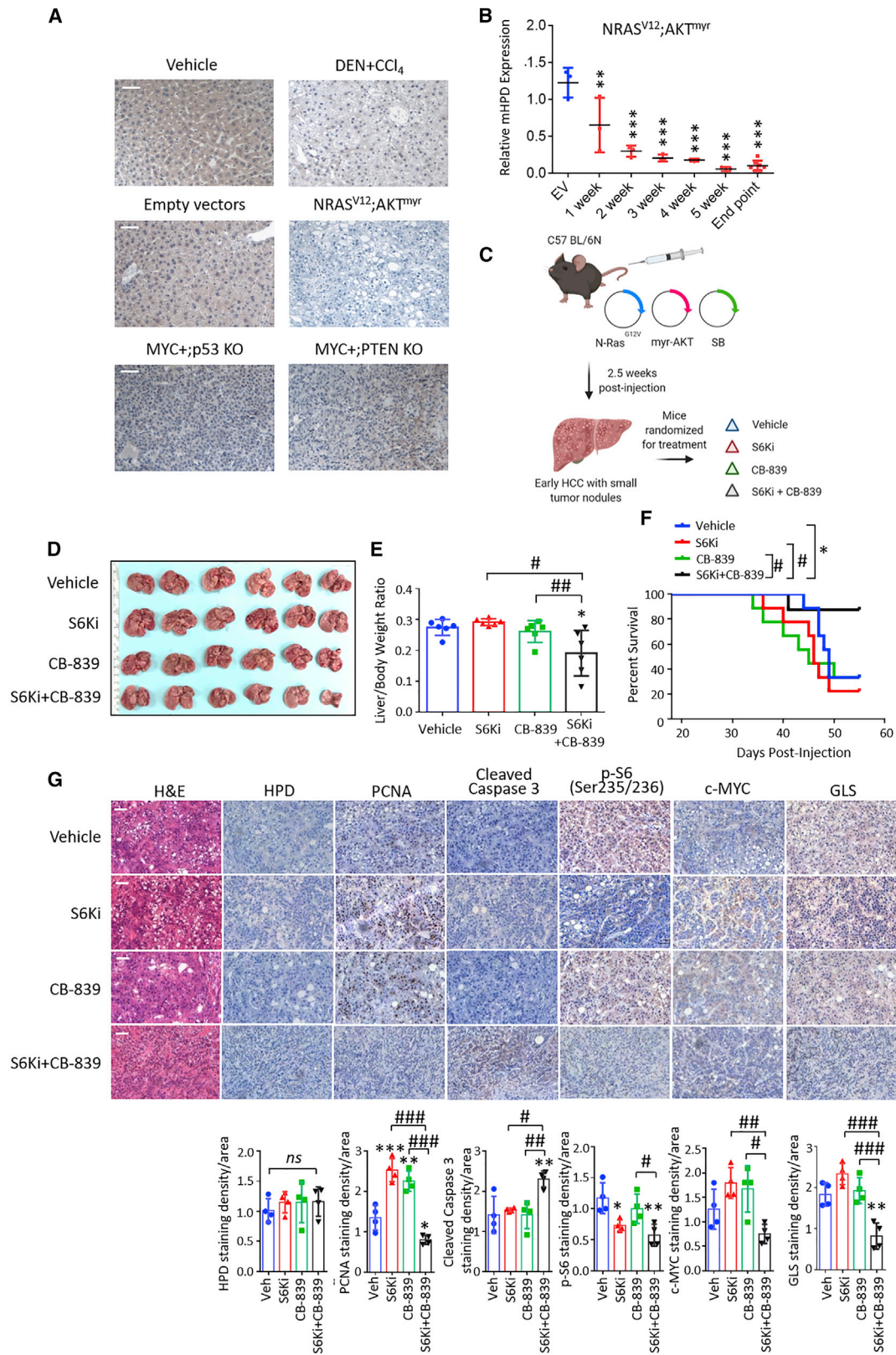
(legend on next page)

proliferation and tumor growth by increasing oxidative pentose phosphate pathway flux, leading to increased RNA biosynthesis and reduced reactive oxygen species (Wang et al., 2019). Metabolic changes are mediated by increased acetyl-coenzyme A (CoA) levels and histone acetylation, which promote histone deacetylase 10 (HDAC10)/glucose-6-phosphate dehydrogenase (G6PD) axis to enhance tumorigenesis (Wang et al., 2019). Unlike what has been observed in lung cancer, our metabolomics results did not show opposite and significant changes in acetyl-CoA levels when HPD was either depleted or overexpressed, suggesting that acetyl-CoA may not play a major role in regulating metabolic changes and nutrient dependency in HCC.

From a disease perspective, the tyrosine catabolic pathway is critical for the regulation of blood tyrosine levels, as the patients with tyrosinemia harboring mutated tyrosine catabolic enzymes present with elevated blood levels of tyrosine (Shiman and Gray, 1998; Scott, 2006). In accordance with the clinical situation of tyrosinemia, we also observed high circulating tyrosine levels in patients with HCC, which is suggestive of its potential diagnostic value in HCC. To incorporate the use of serum tyrosine levels into clinical practice, further evaluation of serum tyrosine with existing HCC diagnostic markers such as α-fetoprotein (Bialecki and Di Bisceglie, 2005) is required to validate its clinical sensitivity and specificity as a surrogate marker for HCC diagnosis and to investigate whether it can guide treatment decisions. In terms of disease management, treatment of tyrosinemia has been largely dependent on nutritional restriction of tyrosine uptake or a low-protein diet, which is less tractable (Scott, 2006). Our findings on the potential therapeutic efficacies of two preclinical drugs (LY2584702 and CB-839) suggest the combinational targeting of mTOR downstream effectors to represent a more manageable treatment option for HCC with impaired tyrosine catabolism. Despite the treatment effects, concerns are raised to the use of micromolar concentrations of CB-839 to achieve synergistic inhibitory effect in our study. A previous study also showed that single CB-839 treatment in most HCC cell lines had very minimal inhibitory effect even when the cells were treated with CB-839 at micromolar concentrations, unlike the nanomolar range of CB-839 being used in other cancers, such as breast and lung cancers (Jin et al., 2020; Gross et al., 2014; Momcilovic et al., 2018). These findings suggest that liver cancer is less responsive toward CB-839 treatment that only targets GLS. It will be worthwhile to evaluate the potential involvement of GLS2, a liver-specific GLS isozyme, in contributing to the less prominent effect of GLS inhibition by CB-839 in HCC. Various GLS inhibitors have been developed and tested in preclinical disease models, among which a dual GLS/GLS2 inhibitor named 968 has shown to have a more potent inhibitory effect and no gross evidence of toxicity (Wu et al., 2018; Lukey et al., 2019). To design an effective combinatorial therapy to target HCC with impaired tyrosine catabolism, it will be important to understand the functional contributions of GLSs and evaluate the therapeutic effects of various GLS inhibitors in combination with p70S6K inhibitors.

STAR★METHODS

Detailed methods are provided in the online version of this paper and include the following:

- KEY RESOURCES TABLE
- RESOURCE AVAILABILITY
  - Lead contact
  - Materials availability
  - Data and code availability
- EXPERIMENTAL MODEL AND SUBJECT DETAILS
  - Cell lines
  - Clinical specimens
  - HCC patient-derived organoids and culture conditions
  - Gene expression profiling and patient samples
  - Animal studies
- METHOD DETAILS
  - Reagents
  - Pathway enrichment analysis
  - RNA extraction and quantitative real-time qPCR
  - Protein extraction and Western Blot
  - Immunohistochemistry
  - Expression plasmids and lentiviral transduction
  - Cell proliferation assay
  - Growth inhibition assay after drug/nutrient depletion treatment
  - Measurement of tyrosine level

Figure 7. Co-targeting of p70S6 kinase and GLS exhibited antitumor effect in a preclinical immunocompetent mouse HCC model

(A) Representative immunohistochemistry images showing HPD expression in resected mouse liver sections of Veh-treated and DEN+CCl$_4$-treated HCC model, and NRAS^{V12};AKT^{myr}-, MYC+;p53 knockout (KO)-, and MYC+;PTEN KO-induced HCC models. Brown color indicates positive staining of HPD expression, and blue color represents the hematoxylin-stained nuclei. Scale bar, 100 μm.

(B) Relative *Hpd* expression in resected liver/tumor tissues from mice at different time pointes after receiving hydrodynamic tail vein injection of NRAS^{V12};AKT^{myr} plasmids.

(C) Schematic of the treatment regimens of single or combination treatment of S6Ki and CB-839 in a N-Ras^{V12};AKT^{myr}-driven HCC immunocompetent mouse model.

(D) Representative images of resected livers from N-Ras^{V12}; AKT^{myr} induced HCC mouse model treated with single or combination treatment of S6Ki and CB-839 (n = 6 mice per group).

(E) Chart showing the liver-to-body weight ratio of resected livers after treatment (n = 6 mice per group). Data are represented as mean ± SD.

(F) Kaplan-Meier survival analysis of mice receiving single or combination treatment of S6Ki and CB-839 (n = 6 mice per group).

(G) Representative H&E images and immunohistochemistry images showing HPD, PCNA, cleaved caspase-3, p-S6, c-MYC, and GLS expression in resected liver sections of N-Ras^{V12};AKT^{myr} HCC mouse model after various treatment regimens. Scale bar, 100 μm. Charts showing the relative staining density of respective proteins. Data are represented as mean ± SD (n = 4 randomly selected fields).

*p < 0.05; **p < 0.01; ***p < 0.001 (versus vehicle treatment). #p < 0.05; ##p < 0.01; ###p < 0.001 (single versus combination treatment).

DEN, N-nitrosodiethylamine; CCl$_4$, carbon tetrachloride; SB, sleeping beauty.

○ Seahorse analysis
○ Metabolite extraction and liquid chromatography-mass spectrometry (LC-MS) analysis
○ Untargeted stable isotopologue tracing of glutamine
● QUANTIFICATION AND STATISTICAL ANALYSIS

AUTHOR CONTRIBUTIONS

M.T. and S.M. conceived the project and designed the experiments. Z.C., H.Z.Z., and Y.Y.Z. designed and carried out all MS-related experiments. M.T. performed the experiments with assistance from T.-L.W., Y.-N.X., C.-H.L., L.Z., N.C., and T.K.-W.L. K.M. and J.-P.Y. consented the patients and provided clinical samples and clinical data information. M.T., S.M., and Z.C. provided funding support and supervised the project. M.T. and S.M. wrote the manuscript.

REFERENCES

Bae, H.R., Kim, D.H., Park, M.H., Lee, B., Kim, M.J., Lee, E.K., Chung, K.W., Kim, S.M., Im, D.S., and Chung, H.Y. (2016). β-Hydroxybutyrate suppresses inflammasome formation by ameliorating endoplasmic reticulum stress via AMPK activation. Oncotarget 7, 66444–66454.

Bialecki, E.S., and Di Bisceglie, A.M. (2005). Diagnosis of hepatocellular carcinoma. HPB (Oxford) 7, 26–34.

Bliss, C.I. (1939). The toxicity of poisons applied jointly. Ann. Appl. Biol. 26, 585–615.

Bott, A.J., Maimouni, S., and Zong, W.X. (2019). The pleiotropic effects of glutamine metabolism in cancer. Cancers (Basel) 11, 770.

Bray, F., Ferlay, J., Soerjomataram, I., Siegel, R.L., Torre, L.A., and Jemal, A. (2018). Global cancer statistics 2018: GLOBOCAN estimates of incidence and mortality worldwide for 36 cancers in 185 countries. CA Cancer J. Clin. 68, 394–424.

Campbell, I. (2006). Liver: metabolic functions. Anaesth. Intensive Care Med. 7, 51–54.

Cancer Genome Atlas Research Network. (2017). Comprehensive and integrative genomic characterization of hepatocellular carcinoma. Cell 169, 1327–1341.e23.

Carracedo, A., Ma, L., Teruya-Feldstein, J., Rojo, F., Salmena, L., Alimonti, A., Egia, A., Sasaki, A.T., Thomas, G., Kozma, S.C., et al. (2008). Inhibition of mTORC1 leads to MAPK pathway activation through a PI3K-dependent feedback loop in human cancer. J. Clin. Invest. 118, 3065–3074.

Csibi, A., Lee, G., Yoon, S.O., Tong, H., Ilter, D., Elia, I., Fendt, S.M., Roberts, T.M., and Blenis, J. (2014). The mTORC1/S6K1 pathway regulates glutamine metabolism through the eIF4B-dependent control of c-Myc translation. Curr. Biol. 24, 2274–2280.

Formisano, L., Napolitano, F., Rosa, R., D'Amato, V., Servetto, A., Marciano, R., De Placido, P., Bianco, C., and Bianco, R. (2020). Mechanisms of resistance to mTOR inhibitors. Crit. Rev. Oncol. Hematol. 147, 102886.

Fouad, Y.A., and Aanei, C. (2017). Revisiting the hallmarks of cancer. Am. J. Cancer Res. 7, 1016–1036.

Fu, L., Dong, S.S., Xie, Y.W., Tai, L.S., Chen, L., Kong, K.L., Man, K., Xie, D., Li, Y., Cheng, Y., et al. (2010). Down-regulation of tyrosine aminotransferase at a frequently deleted region 16q22 contributes to the pathogenesis of hepatocellular carcinoma. Hepatology 51, 1624–1634.

Gross, M.I., Demo, S.D., Dennison, J.B., Chen, L., Chernov-Rogan, T., Goyal, B., Janes, J.R., Laidig, G.J., Lewis, E.R., Li, J., et al. (2014). Antitumor activity of the glutaminase inhibitor CB-839 in triple-negative breast cancer. Mol. Cancer Ther. 13, 890–901.

Hindupur, S.K., González, A., and Hall, M.N. (2015). The opposing actions of target of rapamycin and AMP-activated protein kinase in cell growth control. Cold Spring Harb. Perspect. Biol. 7, a019141.

Ho, C., Wang, C., Mattu, S., Destefanis, G., Ladu, S., Delogu, S., Armbruster, J., Fan, L., Lee, S.A., Jiang, L., et al. (2012). AKT and N-Ras coactivation in the mouse liver promotes rapid carcinogenesis by way of mTOR, FOXM1/SKP2, and c-Myc pathways. Hepatology 55, 833–845.

Huang, A., Yang, X.R., Chung, W.Y., Dennison, A.R., and Zhou, J. (2020). Targeted therapy for hepatocellular carcinoma. Signal Transduct. Target. Ther. 5, 146.

Huch, M., Gehart, H., van Boxtel, R., Hamer, K., Blokzijl, F., Verstegen, M.M., Ellis, E., van Wenum, M., Fuchs, S.A., de Ligt, J., et al. (2015). Long-term culture of genome-stable bipotent stem cells from adult human liver. Cell 160, 299–312.

Jin, H., Wang, S., Zaal, E.A., Wang, C., Wu, H., Bosma, A., Jochems, F., Isima, N., Jin, G., Lieftink, C., et al. (2020). A powerful drug combination strategy targeting glutamine addiction for the treatment of human liver cancer. eLife 9, e56749.

Kinoshita, A., Onoda, H., Fushiya, N., Koike, K., Nishino, H., and Tajiri, H. (2015). Staging systems for hepatocellular carcinoma: Current status and future perspectives. World J. Hepatol. 7, 406–424.

Li, J., Wang, Q., Yang, Y., Lei, C., Yang, F., Liang, L., Chen, C., Xia, J., Wang, K., and Tang, N. (2019). GSTZ1 deficiency promotes hepatocellular carcinoma proliferation via activation of the KEAP1/NRF2 pathway. J. Exp. Clin. Cancer Res. 38, 438.

Liu, S., Cadoux-Hudson, T., and Schofield, C.J. (2020). Isocitrate dehydrogenase variants in cancer - Cellular consequences and therapeutic opportunities. Curr. Opin. Chem. Biol. 57, 122–134.

Llovet, J.M., Zucman-Rossi, J., Pikarsky, E., Sangro, B., Schwartz, M., Sherman, M., and Gores, G. (2016). Hepatocellular carcinoma. Nat. Rev. Dis. Primers 2, 16018.

Lukey, M.J., Cluntun, A.A., Katt, W.P., Lin, M.J., Druso, J.E., Ramachandran, S., Erickson, J.W., Le, H.H., Wang, Z.E., Blank, B., et al. (2019). Liver-type glutaminase GLS2 is a druggable metabolic node in luminal-subtype breast cancer. Cell Rep. 29, 76–88.e7.

Matter, M.S., Decaens, T., Andersen, J.B., and Thorgeirsson, S.S. (2014). Targeting the mTOR pathway in hepatocellular carcinoma: current state and future trends. J. Hepatol. *60*, 855–865.

Momcilovic, M., Bailey, S.T., Lee, J.T., Fishbein, M.C., Braas, D., Go, J., Graeber, T.G., Parlati, F., Demo, S., Li, R., et al. (2018). The GSK3 signaling axis regulates adaptive glutamine metabolism in lung squamous cell carcinoma. Cancer Cell *33*, 905–921.e5.

Mullard, A. (2017). FDA approves first-in-class cancer metabolism drug. Nat. Rev. Drug Discov. *16*, 593.

Nguyen, T.N., Nguyen, H.Q., and Le, D.H. (2020). Unveiling prognostics biomarkers of tyrosine metabolism reprogramming in liver cancer by cross-platform gene expression analyses. PLoS ONE *15*, e0229276.

Noda, C., and Ichihara, A. (1976). Control of ketogenesis from amino acids. IV. Tissue specificity in oxidation of leucine, tyrosine, and lysine. J. Biochem. *80*, 1159–1164.

O'Reilly, K.E., Rojo, F., She, Q.B., Solit, D., Mills, G.B., Smith, D., Lane, H., Hofmann, F., Hicklin, D.J., Ludwig, D.L., et al. (2006). mTOR inhibition induces upstream receptor tyrosine kinase signaling and activates Akt. Cancer Res. *66*, 1500–1508.

Orejuela, D., Jorquera, R., Bergeron, A., Finegold, M.J., and Tanguay, R.M. (2008). Hepatic stress in hereditary tyrosinemia type 1 (HT1) activates the AKT survival pathway in the fah-/- knockout mice model. J. Hepatol. *48*, 308–317.

Palm, W., and Thompson, C.B. (2017). Nutrient acquisition strategies of mammalian cells. Nature *546*, 234–242.

Pavlova, N.N., and Thompson, C.B. (2016). The emerging hallmarks of cancer metabolism. Cell Metab. *23*, 27–47.

Puchalska, P., Martin, S.E., Huang, X., Lengfeld, J.E., Daniel, B., Graham, M.J., Han, X., Nagy, L., Patti, G.J., and Crawford, P.A. (2019). Hepatocyte-macrophage acetoacetate shuttle protects against tissue fibrosis. Cell Metab. *29*, 383–398.e7.

Roessler, S., Jia, H.L., Budhu, A., Forgues, M., Ye, Q.H., Lee, J.S., Thorgeirsson, S.S., Sun, Z., Tang, Z.Y., Qin, L.X., and Wang, X.W. (2010). A unique metastasis gene signature enables prediction of tumor relapse in early-stage hepatocellular carcinoma patients. Cancer Res. *70*, 10202–10212.

Russo, P.A., Mitchell, G.A., and Tanguay, R.M. (2001). Tyrosinemia: a review. Pediatr. Dev. Pathol. *4*, 212–221.

Schulze, K., Imbeaud, S., Letouzé, E., Alexandrov, L.B., Calderaro, J., Rebouissou, S., Couchy, G., Meiller, C., Shinde, J., Soysouvanh, F., et al. (2015). Exome sequencing of hepatocellular carcinomas identifies new mutational signatures and potential therapeutic targets. Nat. Genet. *47*, 505–511.

Scott, C.R. (2006). The genetic tyrosinemias. Am. J. Med. Genet. C. Semin. Med. Genet. *142C*, 121–126.

Shan, C., Lu, Z., Li, Z., Sheng, H., Fan, J., Qi, Q., Liu, S., and Zhang, S. (2019). 4-hydroxyphenylpyruvate dioxygenase promotes lung cancer growth via pentose phosphate pathway (PPP) flux mediated by LKB1-AMPK/HDAC10/G6PD axis. Cell Death Dis. *10*, 525.

Shiman, R., and Gray, D.W. (1998). Formation and fate of tyrosine. Intracellular partitioning of newly synthesized tyrosine in mammalian liver. J. Biol. Chem. *273*, 34760–34769.

Tajiri, K., and Shimizu, Y. (2013). Branched-chain amino acids in liver diseases. World J. Gastroenterol. *19*, 7620–7629.

Tong, M., Che, N., Zhou, L., Luk, S.T., Kau, P.W., Chai, S., Ngan, E.S., Lo, C.M., Man, K., Ding, J., et al. (2018). Efficacy of annexin A3 blockade in sensitizing hepatocellular carcinoma to sorafenib and regorafenib. J. Hepatol. *69*, 826–839.

Wang, X., Yue, P., Tao, H., and Sun, S.Y. (2017). Inhibition of p70S6K does not mimic the enhancement of Akt phosphorylation by rapamycin. Heliyon *3*, e00378.

Wang, X., Shang, Y., Yang, L., Tan, X., Zhang, H., Shan, C., and Liu, S. (2019). HPD overexpression predicts poor prognosis in breast cancer. Pathol. Res. Pract. *215*, 152524.

Wu, C., Chen, L., Jin, S., and Li, H. (2018). Glutaminase inhibitors: a patent review. Expert Opin. Ther. Pat. *28*, 823–835.

Yang, F., Li, J., Deng, H., Wang, Y., Lei, C., Wang, Q., Xiang, J., Liang, L., Xia, J., Pan, X., et al. (2019). GSTZ-1 deficiency activates NRF2/IGF1R axis in HCC via accumulation of oncometabolite succinylacetone. EMBO J. *38*, e101964.

Yang, X., Chen, S.L., Lin, C.S., Liu, L.L., Wang, C.H., and Yun, J.P. (2020). Tyrosine metabolic enzyme HPD is decreased and predicts unfavorable outcomes in hepatocellular carcinoma. Pathol. Res. Pract. *216*, 153153.

Zhu, W.W., Lu, M., Wang, X.Y., Zhou, X., Gao, C., and Qin, L.X. (2020). The fuel and engine: The roles of reprogrammed metabolism in metastasis of primary liver cancer. Genes Dis. *7*, 299–307.

STAR★METHODS

KEY RESOURCES TABLE

REAGENT or RESOURCE	SOURCE	IDENTIFIER
Antibodies		
Rabbit polyclonal anti-HPD	Abcam	Cat#ab133515; RRID: N/A
Rabbit monoclonal anti-p-AMPKα (Thr172)	CST	Cat#2535; RRID: AB_331250
Rabbit polyclonal anti-AMPK	CST	Cat#2532; RRID: AB_330331
Rabbit monoclonal anti-p-mTOR (Ser2448)	CST	Cat#5536; RRID: AB_10691552
Rabbit monoclonal anti-mTOR	CST	Cat#2983; RRID: AB_2105622
Rabbit monoclonal anti-p-p70 S6 Kinase (Thr389)	CST	Cat#8234; RRID: AB_2269803
Rabbit monoclonal anti-p70 S6 Kinase	CST	Cat#2708; RRID: AB_390722
Rabbit monoclonal anti-p-S6 (Ser235/236)	CST	Cat#4858; RRID: AB_916156
Rabbit monoclonal anti-S6	CST	Cat#2217; RRID: AB_331355
Mouse monoclonal anti-c-Myc	Santa Cruz	Cat#sc-40; RRID: AB_2857941
Rabbit monoclonal anti-GLS	Abcam	Cat#ab156876; RRID: AB_2721038
Rabbit monoclonal anti-GLS2	Abcepta	Cat#AP6650D; RRID: AB_10818414
Rabbit monoclonal anti-GS	Abcam	Cat#ab176562; RRID: AB_2868472
Mouse monoclonal anti-β-actin	Sigma-Aldrich	Cat#A5316; RRID: AB_476743
Rabbit polyclonal anti-cleaved Caspase-3	CST	Cat#9661; RRID: AB_2341188
Rabbit polyclonal anti-PCNA	Abcam	Cat#ab18197; RRID: AB_444313
Biological samples		
Human serum samples	Queen Mary Hospital, Hong Kong	N/A
Human HCC patient-derived organoids (HCC#1 and HCC#2)	Dr. Meritxell Huch; Huch et al., 2015	N/A
Human HCC patient-derived organoids (HCC#3 and HCC#4)	This paper	N/A
Chemicals, peptides, and recombinant proteins		
Nitisinone	Sigma-Aldrich	Cat#SML0269; CAS 104206-65-7
DL-β-hydroxybutyrate	Sigma-Aldrich	Cat#H6501; CAS 150-83-4
Acetoacetate	This paper	N/A
L-γ-Glutamyl-p-nitroanilide (GPNA)	Sigma-Aldrich	Cat#G1135; CAS 7300-59-6
LY2584702 (S6Ki)	TargetMol	Cat#T1746; CAS 1082949-68-5
CB-839	BioVision	Cat#B1179; CAS 1439399-58-2
Critical commercial assays		
XFp Cell Mito Stress Test	Aligent	Cat#103010-100
β-Hydroxybutyrate (Ketone Body) Colorimetric Assay Kit	Cayman	Cat#700190
Acetoacetate Assay Kit (Colorimetric)	Abcam	Cat#ab180875
CellTiter-Glo® 2.0 Cell Viability Assay	Promega	Cat#G9242
Tyrosine Colorimetric Assay Kit	BioVision	Cat#K573-100
Deposited data		
NCBI GEO dataset (GSE14520)	Roessler et al., 2010	GEO: GSE14520
TCGA-LIHC	Cancer Genome Atlas Research Network, 2017	TCGA-LIHC
Experimental models: Cell lines		
Hep3B	ATCC	Cat#HB-8064; RRID: CVCL_0326
HepG2	ATCC	Cat#HB-8065; RRID: CVCL_0027

Continued

REAGENT or RESOURCE	SOURCE	IDENTIFIER
PLC/PRF/5	Institute of Virology, Chinese Academy of Medical Sciences	RRID: CVCL_0485
Huh7	JCRB	Cat#JCRB0403; RRID: CVCL_0336
HLE	JCRB	Cat#JCRB0404; RRID: CVCL_1281
MHCC97L	Liver Cancer Institute, Fudan University	RRID: CVCL_4973
MHCC97H	Liver Cancer Institute, Fudan University	RRID: CVCL_4972
MIHA	A gift from Dr. J.R. Chowdhury, Albert Einstein College of Medicine, New York	RRID: CVCL_SA11
293T	ATCC	Cat#CRL-3216; RRID: CVCL_0063
293FT	Invitrogen	Cat#R70007; RRID: CVCL_6911
Experimental models: Organisms/strains		
BALB/cAnN-nu, male	CCMR, HKU	N/A
C57BL/6N, male	CCMR, HKU	N/A
Oligonucleotides		
Human *HPD* qPCR forward primer: 5′-GAAACACGGTGACGGAGTGAA-3′	This paper	N/A
Human *HPD* qPCR reverse primer: 5′-CTCCCGCATGATTTTGGCG-3′	This paper	N/A
Murine *Hpd* qPCR forward primer: 5′-ACAAAGGACCAAAGCCTGAGA-3′	This paper	N/A
Murine *Hpd* qPCR reverse primer: 5′-AGCCCATCTTGTTGCAGTAGA 3′	This paper	N/A
Recombinant DNA		
pLKO.1-puro shRNA plasmid 1 for HPD: 5′-CCGGGGGTAGAGCAAGACAAGTTTGCTCGAGCAAACTTGTCTTGCTCTACCCTTTTTTG-3′	This paper	N/A
pLKO.1-puro shRNA plasmid 2 for HPD: 5′-CCGGCTGGAGATGATCGACCACATTCTCGAGAATGTGGTCGATCATCTCCAGTTTTTG-3′	This paper	N/A
pLKO.1-puro shRNA plasmid for non-target control (NTC): 5′-CCGGCAACAAGATGAAGAGCACAACTCGAGTTGGTGCTCTTCATCTTGTTGTTTTT-3′	This paper	N/A
HPD ORF-Lv105 plasmid	GeneCopoeia	Cat#EX-L2641-Lv105
Lv105-Empty control vector	GeneCopoeia	Cat#EX-NEG-Lv105
Software and algorithms		
R (v3.2.2)	R	https://www.r-project.org/
ImageJ	NIH	https://imagej.nih.gov/ij/index.html
SPSS 21.0	IBM	https://www.ibm.com/products/spss-statistics
GraphPad Prism 6.0	GraphPad Software	https://www.graphpad.com/
Gene Set Enrichment Analysis	Broad Institute	https://www.gsea-msigdb.org/gsea/index.jsp

RESOURCE AVAILABILITY

Lead contact
Further information and requests for reagents and resources should be directed to and will be fulfilled by the lead contact, Stephanie Ma (stefma@hku.hk).

Materials availability

This study did not generate new unique reagents.

Data and code availability

- This paper analyzes existing, publicly available data. These accession numbers for the datasets are listed in the key resources table. Microarray data can be found in the NCBI Gene Expression Omnibus under the accession code GEO: GSE14520.
- This paper does not report original code.
- Any additional information required to reanalyze the data reported in this paper is available from the lead contact upon request.

EXPERIMENTAL MODEL AND SUBJECT DETAILS

Cell lines

HCC cell line Hep3B and human hepatoblastoma cell line HepG2 were purchased from American Type Culture Collection (ATCC). HCC cell line PLC/PRF/5 was obtained from the Institute of Virology, Chinese Academy of Medical Sciences, Beijing, China. HCC cell lines Huh7 and HLE were obtained from Japanese Collection of Research Bioresources (JCRB) Cell Bank. Immortalized normal liver cell line MIHA was provided by Dr. J. R. Chowdhury, Albert Einstein College of Medicine, New York. MHCC97L and MHCC97H cells were obtained from Liver Cancer Institute, Fudan University, China. 293T cells was purchased from ATCC; while 293FT was purchased from Invitrogen. All cell lines used in this study were regularly authenticated by morphological observation and tested for absence of mycoplasma contamination.

Clinical specimens

Venous blood samples were collected from 76 patients with HCC (65 males and 11 females, age ranging from 27-87 years old) and 21 normal control individuals (14 males and 7 females, age ranging from 20-40 years old) from the Department or Surgery, Queen Mary Hospital in Hong Kong. Samples were collected from patients who had not received any previous local or systemic treatment prior to operation. Use of human samples was approved by the committee for ethical review of research involving human subjects at the University of Hong Kong/Hospital Authority Hong Kong West Cluster Institutional Review Board.

HCC patient-derived organoids and culture conditions

Cells were isolated and cultured as previously described (Huch et al., 2015). HCC tissues used for organoid establishment of HCC#3 and HCC#4 were obtained from patients with HCC (HCC#3: male, 64 years old and HCC#4: male, 56 years old) undergoing hepatectomy or liver transplantation at Queen Mary Hospital, Hong Kong, with informed consent obtained from all patients and protocol approved by the University of Hong Kong/Hospital Authority Hong Kong West Cluster Institutional Review Board. Samples were collected from patients who had not received any previous local or systemic treatment prior to operation. HCC patient-derived organoids labeled HCC#1 (male, 69 years old) and HCC#2 (female, 61 years old) were gifts from Dr. Meritxell Huch of The Gurdon Institute at the University of Cambridge.

Gene expression profiling and patient samples

Gene expression profiling studies involving multiple clinical samples were performed analyzing the expression of specific transcripts in two datasets available through Gene Expression Omnibus (GSE14520) of the National Centre for Biotechnology Information (NCBI) and The Cancer Genome Atlas (TCGA) Research Network.

Animal studies

Tumorigenicity was assessed by subcutaneously injection into the flank of 4-weeks old male BALB/c nude mice (n = 5-9 per group). HCC syngeneic model was developed using male C57BL/6N mice through hydrodynamic tail vein injection of plasmids expressing N-Ras, myr-AKT, and sleeping beauty (SB) transposon. In brief, 20μg of plasmids encoding myr-AKT1 and N-Ras along with SB transposase in a ratio of 25:1 were diluted in 2ml saline (0.9% NaCl), filtered through 0.22μm filter and injected into the lateral tail vein of C57BL/6 mice in 5-7 s. The constructs used in this study showed long term expression of genes via hydrodynamic injection (Ho et al., 2012). 18 days after injection of plasmids, mice were randomized for vehicle, S6Ki (25mg/kg/day) alone, CB-839 (100mg/kg/day) alone and combination of S6Ki and CB-839 treatment through oral gavage for 3 weeks. Mice were sacrificed and livers were resected for weight measurement and subsequent histology analysis when treatment was finished. Survival of the remaining mice was monitored for 60 days. All study protocols were approved by and performed in accordance with the Committee of the Use of Live Animals in Teaching and Research at The University of Hong Kong and the Animals (Control of Experiments) Ordinance of Hong Kong.

METHOD DETAILS

Reagents

NTBC (Nitisinone, SML0269), DL-β-hydroxybutyrate, and GPNA (L-γ-Glutamyl-p-nitroanilide, G1135) were purchased from Sigma-Aldrich. S6Ki (LY2584702, T1746) was purchased from TargetMol. CB-839 (B1179) was purchased from BioVision. Acetoacetate was synthesized according to previous publication (Puchalska et al., 2019).

Pathway enrichment analysis

TCGA-LIHC data was downloaded using TCGABiolinks (v2.14) and normalized with DESeq2 (v1.26). Raw data of GSE14520 was downloaded from NCBI and processed with Affy package (v1.64). Differential expression analysis of early stage HCC versus non-tumor livers of TCGA-LIHC and GSE14520 data was performed with limma (v3.42). Differential expressed genes were filtered with adjusted p value < 0.01 and log fold change > 1 or < −1. Gene ontology enrichment analyzed was performed within Cytoscape (v3.8) using BiNGO (v3.0.4) with GO biological process. The resulting GO terms were clustered with AutoAnnotate (v1.3.2) using community cluster (GLay) algorithm. Pathway enrichment analysis was performed using Gene Set Enrichment Analysis (GSEA).

RNA extraction and quantitative real-time qPCR

Total RNA was extracted using RNAisoPlus (Takara) and cDNA was synthesized by PrimeScript RT Master Mix (Takara). qPCR was performed with EvaGreen qPCR MasterMix (ABM) and the following primers: human HPD (forward 5′-GAAACACGGTGACGGAGTGAA-3′ and reverse 5′-CTCCCGCATGATTTTGGCG-3′), murine HPD (forward 5′-ACAAAGGACCAAAGCCTGAGA-3′ and reverse 5′-AGCCCATCTTGTTGCAGTAGA 3′) on a LightCycler 480 II analyzer (Roche) with data analyzed using the LightCycler 480 II software (Roche). β-actin was amplified as an internal control. Relative expression differences were calculated using the $2^{-\Delta\Delta Ct}$ method.

Protein extraction and Western Blot

Protein lysates were quantified and resolved on a SDS-PAGE gel, transferred onto a PVDF membrane (Millipore) and immunoblotted with primary and secondary antibodies. Antibody signal was detected using an enhanced chemiluminescence system (GE Healthcare). The following antibodies were used: HPD (1:500, Abcam, ab133515), p-AMPK (Thr172) (1:1000, Cell Signaling Technology, 2535), AMPK (1:1000, Cell Signaling Technology, 2532), p-mTOR (Ser2448) (1:1000, Cell Signaling Technology, 5536), mTOR (1:1000, Cell Signaling Technology, 2983), p-p70S6 Kinase (Thr389) (1:1000, Cell Signaling Technology, 9234), p70S6 Kinase (1:1000, Cell Signaling Technology, 2708), p-S6 (Ser235/236) (1:1000, Cell Signaling Technology, 4858), S6 (1:1000, Cell Signaling Technology, 2217), c-MYC (1:200, Santa Cruz, sc-40), GLS (1:1000, Abcam, ab156876), GLS2 (1:1000, Abcepta, AP6650D), GS (1:1000, Abcam, ab176562) and β-actin (1:5000, Sigma-Aldrich, A5316). The intensities of the blots were quantified by ImageJ (v1.8.0_112) and the intensities of phosphorylated proteins are calculated and compared against their respective total forms. Western blot analyses were performed in at least two independent experiments and representative results were selected for presentation.

Immunohistochemistry

Immunohistochemical staining of paraffin sections was carried out using a two-step protocol. After antigen retrieval, sections were incubated with anti-human HPD (1:500, Abcam, ab133515), p-S6 (Ser235/236) (1:400, Cell Signaling Technology, 4858), c-MYC (1:200, Santa Cruz, sc-40), GLS (1:100, Abcam, ab156876), cleaved caspase 3 (1:200, Cell Signaling Technology, 9661), PCNA (1:4000, Abcam, ab18197). Anti-rabbit or anti-mouse HRP-labeled polymer (DAKO) was used as secondary antibody. Color detection was performed by liquid DAB+ Substrate Chromogen System (DAKO). Slides were counterstained with Mayer's hematoxylin. Quantification of staining densities of the immunohistochemistry images was performed using ImageJ (v1.8.0_112). Four random fields were selected for quantification.

Expression plasmids and lentiviral transduction

Expression plasmids for shRNAs were made in a pLKO.1-puro vector (Sigma-Aldrich). The targeted sequences were: human HPD (shHPD-1, 5′-CCGGGGGTAGAGCAAGACAAGTTTGCTCGAGCAAACTTGTCTTGCTCTACCCTTTTTTG-3′) and (shHPD-2, 5′-CCGGCTGGAGATGATCGACCACATTCTCGAGAATGTGGTCGATCATCTCCAGTTTTTG-3′) and scrambled shRNA non-target control (NTC) (5′-CCGGCAACAAGATGAAGAGCACAACTCGAGTTGGTGCTCTTCATCTTGTTGTTTTT-3′). Sequences were transfected into 293FT cells, packaged using MISSION Lentiviral Packaging Mix (Sigma-Aldrich). HPD lentiviral overexpression plasmid or empty vector control plasmid were purchased from GeneCopoeia. Sequences were transfected into 293T cells and packaged using Lenti-Pac HIV expression packaging mix (GeneCopoeia). Virus-containing supernatants were collected for subsequent transduction to establish cells with HPD stably repressed or overexpressed. Stable clones were selected with puromycin.

Cell proliferation assay

Cells were seeded on 12-well plates in triplicates. Cells seeded on the plates were trypsinized and the cell number was counted using an automated cell counter (LUNA-II, Logos Biosystems) every day for four days. Cell proliferation of organoid cultures treated with specified concentrations of S6Ki and/or CB-839 for 3 days was evaluated using CellTiter-Glo Luminescent Cell Viability Assay (Promega) according to manufacturer's protocol.

Growth inhibition assay after drug/nutrient depletion treatment

Cells were seeded on 12-well or 24-well plates. Cells were added with specified drugs or changed with either glucose/glutamine depleted medium and cultured for another 4 days. Cells were fixed with paraformaldehyde and stained with 2% crystal violet. 10% acetic acid was added to the stained cells to dissolve the dye. The intensity of the dye was measured by absorbance at 595nm.

Measurement of tyrosine level

Human serum samples were deproteinized by passing through Amicon Ultra-0.5mL centrifugal column (Millipore). Tyrosine levels were measured using Tyrosine Colorimetric Assay Kit (BioVision) according to the manufacturer's protocol.

Seahorse analysis

Mitochondrial function was determined by measuring oxygen consumption rate (OCR) of each cell line using XF Cell Mito Stress Test Kit (Agilent Technologies). HCC cell lines were seeded in an XF24 cell culture microplate. The sensor cartridge and base medium were prepared by adding 1mM pyruvate, 2mM glutamine and 10mM glucose. Seahorse assay was run in XFe24 Extracellular Flux Analyzer (Agilent Technologies). Following three baseline OCR measurements, cells were exposed sequentially to oligomycin ($0.5\mu M$), carbonyl cyanide-4 (trifluoromethoxy) phenylhydrazone (FCCP) ($1\mu M$), and rotenone/antimycin A ($0.5\mu M$). Three measurements were recorded after every injection. To normalize the results, protein concentrations per well was quantified with Bradford assay (Bio-Rad). The assay results were analyzed using Wave program 2.3.0 (Seahorse Bioscience).

Metabolite extraction and liquid chromatography-mass spectrometry (LC-MS) analysis

5×10^6 cells were plated in 15cm dish (three replicates per cell line) with metabolites extracted after 48 hours using 80% methanol. Cells were quickly washed twice with ice-cold PBS and water, followed by metabolite extraction using $-70°C$ 80:20 methanol:water (LC-MS grade methanol, Fisher Scientific). The cell-methanol mixture was subjected to three freeze-thaw cycles. Extracts were centrifuged for 15min at 5000rpm to pellet insoluble material and supernatants were transferred to clean tubes. The extraction procedure was repeated once and all supernatants were pooled, dried for evaporation under vacuum and stored at $-80°C$ until analysis. The methanol-insoluble protein pellet was solubilized in 0.2M NaOH at 95°C for 20min and quantified using the BioRad Bradford assay. On the day of metabolite analysis, dried cell extracts were reconstituted in 70% acetonitrile at a relative protein concentration of $1\mu g/ml$ and reconstituted extract was injected for LC-MS-based untargeted metabolite profiling.

Untargeted stable isotopologue tracing of glutamine

5×10^6 cells were cultured in complete DMEM. 48 hours after cell seeding, cells were rinsed twice with PBS and medium was changed to glutamine free DMEM supplemented with dialyzed FBS and 2 mM $^{13}C_5$-labeled glutamine for specified time intervals. Intracellular metabolites were extracted and analyzed as mentioned above.

QUANTIFICATION AND STATISTICAL ANALYSIS

For public dataset analysis, R language (package version 3.2.2) and Bioconductor were used for background correction, normalization, calculation of gene expression and gene annotation. Survival curves were plotted by the Kaplan-Meier method and the statistical p values were generated by the Cox-Mantel log-rank test. Multivariate Cox proportional hazards regression was used to evaluate independent clinical variables on patient survival. *In vitro* functional assays were performed in at least three independent experiments with three technical replicates. Data were analyzed by SPSS 21.0 or GraphPad Prism 6.0 and shown as mean ± standard deviations, unless otherwise specified. The statistical details of the experiments can be found in the figure legends. Differences between groups were analyzed by Student's t test or one-way ANOVA. Drug interaction was evaluated the Bliss independence model (Bliss, 1939). Based on the Bliss independence model, the expected growth inhibition (Eexp) brought by drug combination (A + B) is given by: Eexp = Ea +Eb -Ea × Eb, where Ea is the growth inhibition brought by drug A alone, and Eb is the growth inhibition brought by drug B alone. The difference between the expected (Eexp) and the observed (Eobs) growth inhibition was calculated. When ΔE (Eobs – Eexp) > 5, the two drugs are considered to be interacting synergistically. Statistical significance was defined as $p < 0.05$. $^*p < 0.05$, $^{**}p < 0.01$ and $^{***}p < 0.001$; $^\#p < 0.05$, $^{\#\#}p < 0.01$ and $^{\#\#\#}p < 0.001$.